AFRL-RB-WP-TP-2010-3023

FEEDBACK FLOW CONTROL FOR A PITCHING TURRET (PART I) (POSTPRINT)

T. Vaithianathan and H.A. Carlson

Clear Science Corp.

R.D. Wallace, P.R. Shea, and M.N. Glauser

Syracuse University

JANUARY 2010

AIR FORCE RESEARCH LABORATORY
AIR VEHICLES DIRECTORATE
WRIGHT-PATTERSON AIR FORCE BASE, OH 45433-7542
AIR FORCE MATERIEL COMMAND
UNITED STATES AIR FORCE

REPORT DOCUMENTATION PAGE

Form Approved
OMB No. 0704-0188

1. REPORT DATE *(DD-MM-YY)*	2. REPORT TYPE	3. DATES COVERED *(From - To)*
January 2010	Conference Paper Postprint	07 April 2008 – 23 November 2009

4. TITLE AND SUBTITLE
FEEDBACK FLOW CONTROL FOR A PITCHING TURRET (PART I) (POSTPRINT)

5a. CONTRACT NUMBER
FA8650-08-C-3827

5b. GRANT NUMBER

5c. PROGRAM ELEMENT NUMBER
0605502

6. AUTHOR(S)
T. Vaithianathan and H.A. Carlson (Clear Science Corp.)
R.D. Wallace, P.R. Shea, and M.N. Glauser (Syracuse University)

5d. PROJECT NUMBER
A0DX

5e. TASK NUMBER

5f. WORK UNIT NUMBER
0C

7. PERFORMING ORGANIZATION NAME(S) AND ADDRESS(ES)

Clear Science Corp.
663 Owego Hill Road
Harford, NY 13784-0233

Syracuse University
Department of Mechanical and Aerospace Engineering
223 Link Hall
Syracuse, NY 13244

8. PERFORMING ORGANIZATION REPORT NUMBER

9. SPONSORING/MONITORING AGENCY NAME(S) AND ADDRESS(ES)
Air Force Research Laboratory
Air Vehicles Directorate
Wright-Patterson Air Force Base, OH 45433-7542
Air Force Materiel Command
United States Air Force

10. SPONSORING/MONITORING AGENCY ACRONYM(S)
AFRL/RBCA

11. SPONSORING/MONITORING AGENCY REPORT NUMBER(S)
AFRL-RB-WP-TP-2010-3023

12. DISTRIBUTION/AVAILABILITY STATEMENT
Approved for public release; distribution unlimited.

13. SUPPLEMENTARY NOTES
Conference presentation published in the Proceedings of the 48th AIAA Aerospace Sciences Meeting Including the New Horizons Forum and Aerospace Exposition, 4 - 7 January 2010, Orlando, FL. PAO Case Number: 88ABW-2009-5009; Clearance Date: 02 Dec 2009. Paper contains color.

14. ABSTRACT
Closed-loop systems have been developed for controlling the flow above a three-dimensional turret. The top of the turret is hemispherical, houses a flat optical aperture, and can rotate about two axes (pitch and yaw). The extent of separation and concomitant turbulence levels in the flow above the aperture change as the turret rotates. The control objective is to minimize the separation and turbulence in the dynamic environment created by the articulating turret. The closed-loop control systems include dynamical and measurement-based estimators, regulators, filters, and compensators. These components are developed using both computational data from CFD simulations and experimental data from wind tunnel runs within the common framework of SMARTflow—engineering software for flow control system design. The control systems are evaluated through a series of control-in-the-loop CFD simulations and wind tunnel runs, demonstrating the merits of feedback control through robustness in the presence of measurement noise, modeling errors, and highly unsteady conditions and through reductions in actuation energy below levels required by open-loop systems. Controller designs and computational tests are described here; wind tunnel tests are described in the companion paper.

15. SUBJECT TERMS
aerodynamic flow control, feedback flow control, turret, feedback control, separation control

16. SECURITY CLASSIFICATION OF:			17. LIMITATION OF ABSTRACT:	18. NUMBER OF PAGES	19a. NAME OF RESPONSIBLE PERSON (Monitor)
a. REPORT	b. ABSTRACT	c. THIS PAGE			James H. Myatt
Unclassified	Unclassified	Unclassified	SAR	20	19b. TELEPHONE NUMBER *(Include Area Code)* N/A

Standard Form 298 (Rev. 8-98)
Prescribed by ANSI Std. Z39-18

48th AIAA Aerospace Sciences Meeting Including the New Horizons Forum and Aerospace Exposition
4 - 7 January 2010, Orlando, Florida
AIAA 2010-360

Feedback Flow Control for a Pitching Turret (Part I)

T. Vaithianathan* and H. A. Carlson†
Clear Science Corp., Harford, NY, USA

R. D. Wallace,‡ P. R. Shea,‡ and M. N. Glauser§
Syracuse University, Syracuse, NY, USA

Closed-loop systems have been developed for controlling the flow above a three-dimensional turret. The top of the turret is hemispherical, houses a flat optical aperture, and can rotate about two axes (pitch and yaw). The extent of separation and concomitant turbulence levels in the flow above the aperture change as the turret rotates. The control objective is to minimize the separation and turbulence in the dynamic environment created by the articulating turret. The closed-loop control systems include dynamical and measurement-based estimators, regulators, filters, and compensators. These components are developed using both computational data from CFD simulations and experimental data from wind tunnel runs within the common framework of SMARTFLOW—engineering software for flow control system design. The control systems are evaluated through a series of control-in-the-loop CFD simulations and wind tunnel runs, demonstrating the merits of feedback control through robustness in the presence of measurement noise, modeling errors, and highly unsteady conditions and through reductions in actuation energy below levels required by open-loop systems. Controller designs and computational tests are described here; wind tunnel tests are described in the companion paper, "Feedback Flow Control for a Pitching Turret (Part II)."

I. Introduction

TURBULENCE, random density fluctuations, and aero-optical distortion in the flow around a turret can degrade the performance of a laser system housed within the turret. Laser light passing through the turbulent region is refracted by variations in density and optical path differences, scattering the light and reducing the laser intensity. One solution to the problem is to adapt the optical system in a way that compensates for the flow distortion—without altering the flow itself; for example, a morphing lens that keeps the laser focused in the presence of aero-optic distortions through contortions of the deformable mirror.[1] Another solution is to control (minimize)—either actively or passively—the flow fluctuations that cause aero-optical distortion.

In a passive flow control experiment, vortex generators mounted on the upstream side of a two-dimensional turret successfully reduced distortions at certain aperture angles of attack.[2] In another experiment, a spanwise array of synthetic jet actuators actively reduced flow fluctuations and delayed separation on a three-dimensional turret.[3] In an open-loop control experiment, synthetic jets were used to reduce the root-mean-square (rms) values of fluctuating velocity in the turbulent flow around a three-dimensional turret.[4]

Closed-loop control systems are designed to improve performance over open-loop systems through robustness, the ability to compensate for uncertainties over a range of flight conditions, and by achieving more with less—reducing actuator power, size, and weight requirements. A closed-loop system utilized synthetic jets to delay the onset of stall on a NACA 4412 airfoil, consuming less power than an open-loop system that increased stall angle by the same amount.[5,6] More recently, a proportional feedback controller was used to modulate synthetic jets on a 3D turret and reduce fluctuation levels in the wake.[7] The tests were performed

*Research Scientist, Clear Science Corp., 663 Owego Hill Road, Harford, NY 13784-0233.
†President, Clear Science Corp., 663 Owego Hill Road, Harford, NY 13784-0233, AIAA Associate Fellow.
‡Graduate Student, Syracuse University, Dept. Mech. & Aero. Engr., Syracuse, NY 13244-1240, AIAA Student Member.
§Professor, Syracuse University, Dept. Mech., Aero. &Manuf. Engr., Syracuse, NY 13244-1240, AIAA Associate Fellow.

at Mach 0.3 in the Subsonic Aerodynamic Research Laboratory (SARL) wind tunnel at Wright-Patterson Air Force Base, OH.

Here, closed-loop flow control tests have been performed with a 3D turret at Mach 0.1. Compressible effects are not present at this speed, but systems for controlling velocity fluctuations in incompressible flows will be effective in controlling density fluctuations at higher speeds because of the strong correlation between velocity and density fluctuations.[8] Both computational and experimental tests were performed. The computational tests are described in "Feedback Flow Control for a Pitching Turret (Part I)." This paper also describes the controller designs, which are first demonstrated computationally and then tested experimentally in the wind tunnel. The experimental tests are described in "Feedback Flow Control for a Pitching Turret (Part II)."

II. Problem Description

The control problem involves fully turbulent, incompressible flow past a three-dimensional (3D) turret, and the control objective is to minimize levels of separation and velocity fluctuations above the aperture. Free stream conditions in the computational simulations and the wind tunnel conditions in the experiment are approximately equal. The nominal free stream Reynolds number based on the diameter of the turret is 450,000, and the free stream Mach number is 0.1. The computational model of the turret and the wind tunnel test article also match—with some differences in the details. The turret consists of a six-inch-diameter hemisphere mounted on a six-inch-diameter cylinder. The cylinder is four inches in height and is mounted on a splitter plate. A flat aperture, 2.8 inches in diameter, is located at the top of the turret. The top, hemispherical section can rotate within the cylindrical stand in two directions: pitch and yaw. Rotation about the pitch axis alone is examined here.

The pitch angle is defined as the angle between a vector normal to the aperture and the free stream vector. When the normal is aligned with the turret centerline, the pitch angle is 90°. As the flat aperture pitches back, it becomes a backward facing ramp, separation levels increase as the pitch angle increases, and this increases levels of velocity fluctuations in the flow above and downstream of the aperture. The objective is to manage and minimize the separation and concomitant fluctuations in the aperture field of view as the pitch angle is varied sinusoidally.

Because of limitations in resolving all the scales of the turbulent flow in the computational model, there are differences between the simulated flow and the flow in the wind tunnel tests. Velocity fluctuation levels are significantly higher in the wind tunnel tests than they are in the computational simulations. Also, using the same rotational rates and amplitudes in the computational simulations that are imposed in the wind tunnel would result in extremely long simulation times because of the model size and the small time step size required for temporal accuracy.

Therefore, the pitch rate imposed in the simulations is considerably higher—and the range of motion lower—in order to facilitate multiple simulations for controller design, calibration, and testing within a reasonable time frame. The strategy is to use control-in-the-loop CFD simulations to develop and evaluate control methods and designs that are then applied in the wind tunnel. The CFD and wind tunnel controllers are comprised of the same components (described in Section IV); however, these components are calibrated with CFD data for the control simulations and are calibrated with experimental data for the control tests in the wind tunnel. The intent is not to use experimental data to validate CFD models and methods but rather to develop and evaluate closed-loop control designs for the wind tunnel through CFD simulations.

III. The CFD Model

The CFD model employs the method of Detached Eddy Simulation (DES), first proposed by Spalart *et. al* and applicable to turbulent flows—particularly flows with separation.[9] Large Eddy Simulation (LES) is an alternative method that uses filters to resolve some (but not all) of the length scales in a turbulent flow.[10] This requires a considerably finer grid than a Reynolds-Averaged Navier-Stokes (RANS) model does, because the RANS model resolves only the mean flow. LES can become computationally expensive in many problems involving high Reynolds number flows with a large range in scales. DES provides a compromise between fidelity and expense by resolving larger eddies in the outer flow where separation-induced structures reside and reverting to the RANS model in the wall region where length scales are very small. The CFD code is CFL3D,[11] and a one-equation, Spalart-Allmaras (S-A) turbulence model is applied in the wall region.[12]

The S-A model contains a destruction term, which is proportional to $(\tilde{\nu}/d)^2$ where d is the distance to the wall and $\tilde{\nu}$ is the eddy viscosity. When balanced with the production term, this term adjusts the eddy viscosity to scale with the local deformation rate (S) and d: $\tilde{\nu} \propto Sd^2$. Sub-grid-scale (SGS) eddy viscosities are proportional to S and the grid spacing Δ: $\tilde{\nu}_{\text{SGS}} \propto S\Delta^2$. The S-A SGS model is obtained by replacing d with a length scale Δ that is proportional to the grid spacing. The model used in the DES formulation is obtained by replacing the length scale of the S-A destruction term to be the minimum of Δ and the distance to the closest wall: $\tilde{d} \equiv \min(d, C_{\text{DES}}\Delta)$ where $\Delta \equiv \max(\Delta x_1, \Delta x_2, \Delta x_3)$ and $C_{\text{DES}} = 0.65$.

Figure 1 contains views of the CFD grid. The left panel of Figure 1 contains a projection of the grid onto the lower boundary of the computational domain. The other outer boundaries are located 15 turret diameters from the turret surface in a radial direction. The middle panel of the figure contains a projection of the grid onto the turret surface. The centerline of the turret is coincident with the x_2-axis. The right panel contains a slice of the grid on the centerplane. The turret is symmetric about this plane, but symmetry is not imposed. The full domain is modeled in order to accommodate rotations in the yaw direction (about the x_2 axis). The grid is structured with a total of 14.68 million points. The wall spacing is 1×10^{-4} inches, yielding $y^+ \sim 0.8$ at a Reynolds number of 450,000. The spatial resolution is finer in the region around the aperture in order to adequately resolve the separated flow with DES.

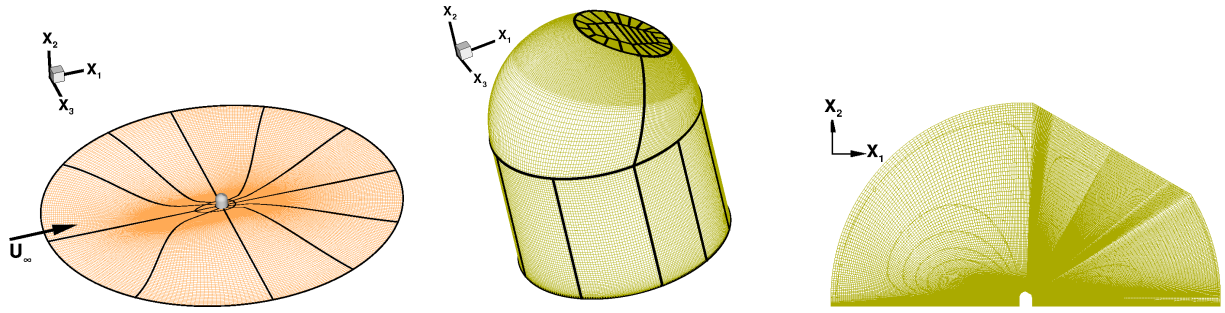

Figure 1. Views of the 3D CFD grid. Projections of the grid onto the bottom boundary (left), the turret surface (middle), and the centerplane (right).

In the control simulations, the turret pitches sinusoidally about the x_3 axis only, according to the following prescribed function:

$$\theta(t) = \theta_0 + \Delta\theta \left(\frac{\pi}{180}\right) \sin\left[\left(\frac{2\pi k_r}{L_{ref}}\right) t\right]. \tag{1}$$

θ_0 is the nominal pitch angle of $2\pi/3$ or 120°: the angle between a line normal to the aperture and the freestream flow direction ($+x_1$ axis). $\Delta\theta = 1°$ yields an oscillation range between 119° and 121°. k_r is the reduced frequency ($k_r = 0.0415$), and $L_{ref} = 6$ inches. The dimensionless time in (1) is non-dimensionalized by L_{ref} and the free stream speed of sound. Differentiating (1) with respect to time yields a maximum pitch rate of 587 degrees per second.

IV. Controller Design

The components of the feedback control system are constructed with Clear Science Corp.'s flow-control-system-design software—SMARTFLOW—and are identified in the flowchart of Figure 2. Designing the system begins with an ensemble of CFD solutions from a time-accurate simulation (or simulations) of unsteady flow. Here, the high-dimensional CFD model is the *plant*. When the system is based on wind tunnel test data, then high-resolution instrumentation constitutes the plant: a Particle Image Velocimetry (PIV) system. The following sections describe the components of the system that is used in both control-in-the-loop CFD simulations and wind tunnel tests.

A. Control Input and Performance Output

In general, control input is a set of surface jet velocities, $\zeta_{(\rho)}(t)$, produced by a collection of surface actuators. $\zeta_{(\rho)}$ is the velocity magnitude corresponding to a specific actuator or actuator set on the turret—denoted by "ρ." As the term implies, an actuator set may be composed of more than one actuator but may operate in

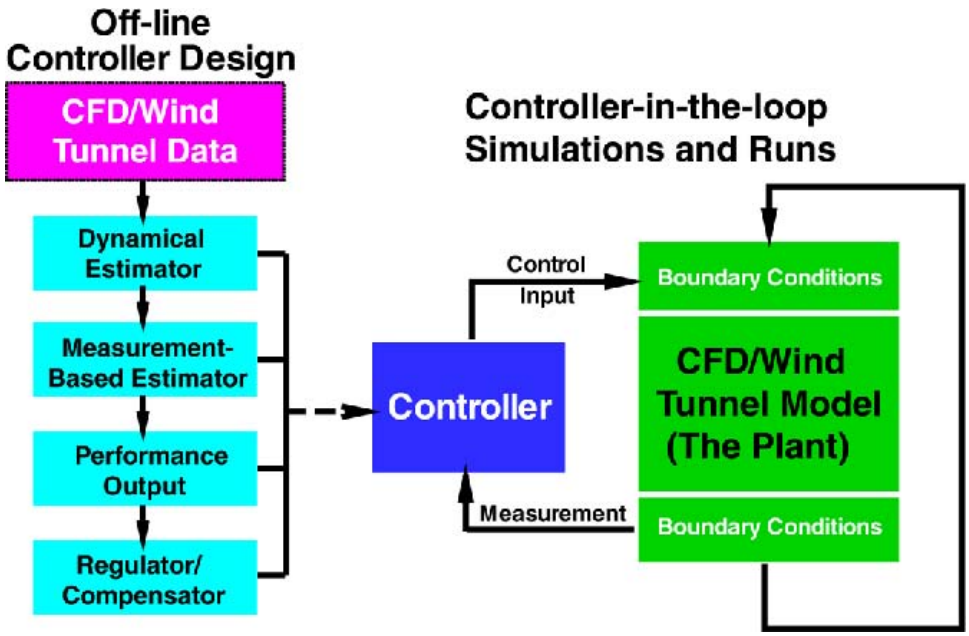

Figure 2. Flow chart of SMARTFLOW**—the flow control system design software.**

tandem, representing a single control input. For example, one row of actuators may be defined as a single input. Alternatively, a row of N actuators may be defined as N inputs operating independently. Here, the control input corresponds to suction jets at the locations identified in Figure 3. Slot locations in the wind tunnel test article are constrained by the availability of plumbing space inside the turret. The slot are located closer to the aperture in the CFD model, because actuation is more effective at this location, and the greater degree of effectiveness is required in the simulations.

Slots located on upstream side of the flat aperture pull momentum toward the turret and counteract the separation that occurs as the flow crosses over the aperture. Suction velocity is modulated by the controller as the levels of separation rise and fall due to the change in pitch angle. The slots operate as a single unit in both the CFD and wind tunnel tests. The jet momentum coefficient is

$$c_\mu \equiv \frac{u_{\text{jet}}}{U_\infty}\frac{A_{\text{jet}}}{A_a} \tag{2}$$

where u_{jet} is the jet amplitude, U_∞ is the free stream velocity, A_{jet} is the total jet area, and A_a is the area of the aperture. The aperture radius is $r_a = 1.4$ inches, and the area is $A_a = \pi r_a^2$. The sizes of each CFD and experimental jet slot are equivalent.

The jet velocity that counteracts separation at a nominal pitch angle in open-loop wind tunnel runs is $c_\mu = -6.8 \times 10^{-4}$ per slot. To achieve the same level of control in the CFD simulations requires a fourfold increase in suction velocity with a momentum coefficient of $c_\mu = -2.77 \times 10^{-3}$ per slot. The control input used by the regulator or compensator is actually the rate of change in suction velocity, rather than the velocity itself. Motivation for this choice and the specific definition are described in Section C.

Again, the control objective is to minimize levels of separation and velocity fluctuations above the aperture. The performance output should be a measure of these levels. Control then becomes a tracking problem with the controller maintaining, or tracking, a value of the performance output that corresponds to low levels of separation and velocity fluctuations. Flow begins to separate when the wall-normal velocity gradient at the wall approaches zero. The viscous component of force acting on the turret surface is a function of the velocity gradients and wall shear stresses through the constitutive relation. The streamwise component of viscous force, or integrated shear stress, acting on the aperture surface (Ω) is

$$F_V^1 = \frac{\varpi}{2}\int\left(\frac{\partial u^l}{\partial x^1} + \frac{\partial u^1}{\partial x^l}\right) n^l \, d\Omega. \tag{3}$$

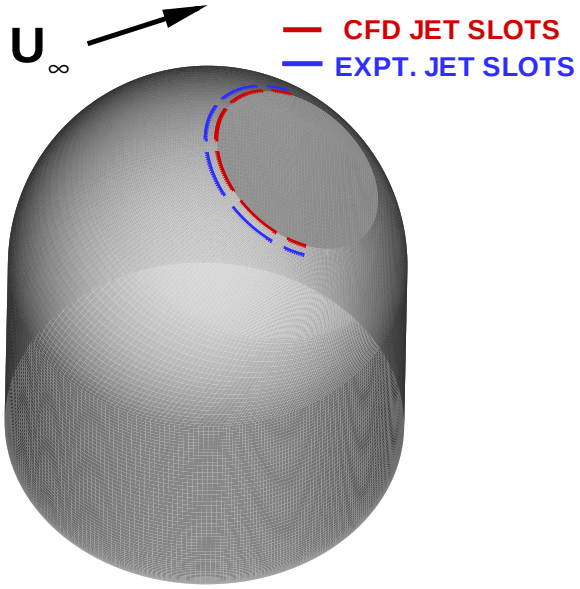

Figure 3. Jet slot locations in the CFD model (red) and the wind tunnel test article (blue).

where $\varpi = 2Ma_\infty/Re_\infty$ and n^l is the l component of the surface normal.

An initial control test utilized values of the performance output computed by the high-dimensional CFD model. These CFD data will not be available in practical applications, but the initial tests are designed to evaluate the performance of regulators. In the actual control-in-the-loop simulations, the performance output is approximated by low-dimensional estimators. In both the initial and final tests, the output is defined as integrated shear stress: $y = F_{\mathrm{V}}^1$. The target value of the output is equal to the time-averaged integrated shear stress for which the flow is attached: $y_T = 0.0362$. Lower, more negative values of the shear stress, integrated over the aperture surface, correspond to higher levels of separation above the surface; therefore, increasing F_V^1 will reduce separation.

Figure 4 contains results from the initial control run with CFD-computed output in the loop: time histories of performance output in the left panel and control input in the right. From the red curve in the left panel, fluctuations in the output are small when the turret is stationary at the nominal pitch angle; the value is slightly negative. For the pitching turret without actuation (blue curve), oscillations in output are significant with values dipping below -0.02 when the turret is pitched fully back. From the green curve in the left panel, open-loop control raises the mean value of output, but the oscillation levels actually increase, even though positive values are maintained. In the open-loop simulation, the suction jet is steady with a momentum coefficient of $c_\mu = -0.0138$ (the green curve in the right panel of Figure 4). From the purple curve in the left panel, the closed-loop controller produces lower oscillations in output than the open-loop controller. From the purple curve in the right panel, it does so with fairly large changes in control input, which varies between values of -0.002 and -0.04.

B. Low-Dimensional Estimators

Deployable feedback systems that control in real time will have to rely on models that are much more computationally efficient than the high-dimensional CFD model. To that end, two types of low-dimensional state estimators have been developed and tested: measurement-based and dynamical. Used together, these two components form a compensator and Kalman filter for dealing with uncertainties and noise, as described in Section C. The system state is defined as a perturbation velocity—$\acute{u}^i(\boldsymbol{x}, t)$. A low-dimensional approximation of $\acute{u}^i(\boldsymbol{x}, t)$ is derived by the method of proper orthogonal decomposition (POD).[13]

A correlation tensor is constructed using N snapshots (solutions) of the unsteady flow at $t = t_{(1)}, t_{(2)}, ...,$

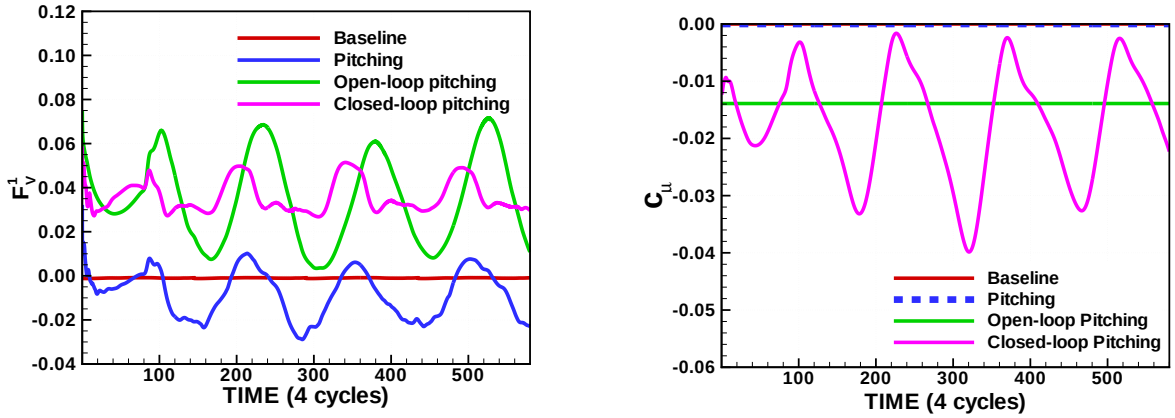

Figure 4. Time histories of performance output (left panel) and control input (right panel) from simulations with no actuation (red and blue curves), an open-loop control simulation (green curves), and a closed-loop control simulation with CFD-computed output in the loop (purple curves).

$t_{(N)}$:

$$R_{(mn)} = \int_\Omega \acute{u}^i_{(m)}(\boldsymbol{x})\acute{u}^j_{(n)}(\boldsymbol{x})d\boldsymbol{x} \quad (m,n=1,...,N)\,, \tag{4}$$

with $\acute{u}^i_{(m)}(\boldsymbol{x}) = \acute{u}^i(\boldsymbol{x},t_{(m)})$ denoting the ith contravariant component of perturbation velocity from snapshot m (a single solution at a particular time step from an unsteady CFD simulation). Constructed in this manner, the eigenvectors of $R_{(mn)}$ maximize the mean square projection of the flow velocity, represented as

$$\acute{u}^i(\boldsymbol{x},t) = a_{(n)}(t)\phi^i_{(n)}(\boldsymbol{x}) \tag{5}$$

where

$$a_{(n)}(t) = \int_\Omega \acute{u}^i(\boldsymbol{x},t)\phi^{(n)}_i(\boldsymbol{x})d\boldsymbol{x}\,, \tag{6}$$

Using 51 snapshots from an unsteady simulation to construct the POD model, 98% of the kinetic energy in the flow is represented in just two POD modes. The time-dependent coefficients of these two modes, $a_{(1),(2)}(t)$, form the state estimates that are used by both the dynamical and measurement-based estimators.

The dynamical estimator is derived by projecting the momentum conservation equation (a partial differential equation, PDE) onto a low-dimensional set of POD eigenvectors, producing a set of coupled ordinary differential equations (ODEs):

$$\begin{aligned}\frac{da_{(n)}}{dt} = {} & \alpha^{<0000>}_{(n)} + \varpi\alpha^{<1000>}_{(n)} + \left(\alpha^{<0010>}_{(n)(\mu)} + \varpi\alpha^{<1010>}_{(n)(\mu)}\right)\dot{\eta}_{(\mu)} + \alpha^{<0001>}_{(n)(\mu)}\frac{d\dot{\eta}_{(\mu)}}{dt} \\ & + \alpha^{<0020>}_{(n)(\mu\nu)}\dot{\eta}_{(\mu)}\dot{\eta}_{(\nu)} + \left(A^{<0100>}_{(np)} + \varpi A^{<1100>}_{(np)} + A^{<0110>}_{(np)(\mu)}\dot{\eta}_{(\mu)}\right)a_{(p)} + A^{<0200>}_{(npq)}a_{(p)}a_{(q)} \\ & + \left(\beta^{<0100>}_{(n)(\rho)} + \varpi\beta^{<1100>}_{(n)(\rho)} + \beta^{<0110>}_{(n)(\rho)(\mu)}\dot{\eta}_{(\mu)} + B^{<0200>}_{(np)(\rho)}a_{(p)}\right)\zeta_{(\rho)} + \beta^{<0001>}_{(n)(\rho)}\frac{d\zeta_{(\rho)}}{dt} + \beta^{<0200>}_{(n)(\rho\sigma)}\zeta_{(\rho)}\zeta_{(\sigma)}.\end{aligned} \tag{7}$$

The system in (7) contains linear and bi-linear terms involving $a_{(n)}$, $\zeta_{(\rho)}$, and $\dot{\eta}_{(\mu)}$. The POD coefficient $a_{(n)}$ is the dependent variable, $\zeta_{(\rho)}$ is the surface jet magnitude, and $\dot{\eta}_{(\mu)}$ is a modal representation of surface velocity due to rotation of the turret. In the case of the pitching turret with only one rotational degree of freedom, $\mu = 1$ and $\eta = \theta$. $\alpha^{<0000>}_{(n)}$, $\alpha^{<1000>}_{(n)}$, $\alpha^{<0010>}_{(n)(\mu)}$, $\alpha^{<1010>}_{(n)(\mu)}$, $\alpha^{<0001>}_{(n)(\mu)}$, $\alpha^{<0020>}_{(n)(\mu\nu)}$, $A^{<0100>}_{(np)}$, $A^{<1100>}_{(np)}$, $A^{<0110>}_{(np)(\mu)}$, $A^{<0200>}_{(npq)}$, $\beta^{<0100>}_{(n)(\rho)}$, $\beta^{<1100>}_{(n)(\rho)}$, $\beta^{<0110>}_{(n)(\rho)(\mu)}$, $B^{<0200>}_{(np)(\rho)}$, $\beta^{<0001>}_{(n)(\rho)}$, and $\beta^{<0200>}_{(n)(\rho\sigma)}$ are time-invariant coefficients that are computed once during the model construction phase.

A linear dynamical estimator is formed by simply excluding the bi-linear terms in (7):

$$\dot{\hat{\boldsymbol{x}}} = \boldsymbol{a}_0 + \boldsymbol{A}_1\hat{\boldsymbol{x}} + \boldsymbol{b}_0 u + \boldsymbol{b}_2\dot{u} + \boldsymbol{b}_3\dot{\eta} + \boldsymbol{b}_4\ddot{\eta} \tag{8}$$

where regular letters denote scalars, bold lower-case letters denote vectors and bold upper-case letters denote matrices. The vector $\hat{\boldsymbol{x}}$ is composed of POD coefficients, and the dynamical model in (8) predicts the evolution in time of those coefficients.

Another important component of the control system is a measurement-based estimator, which correlates the flow dynamics around a surface with discrete measurements taken on the surface.[14,15] Pressure measurements are used here. The key is that the measured quantity correlates with the state estimate (the POD coefficients). The estimated POD coefficient may be written as a series expansion with successive terms containing increasing powers of the pressure:

$$\tilde{a}_{(n)}(t;t) = B_{(ni)}p_{(i)}(t) + C_{(nij)}p_{(i)}(t)p_{(j)}(t) + D_{(nijk)}p_{(i)}(t)p_{(j)}(t)p_{(k)}(t) + \cdots \tag{9}$$

This may be truncated to include only the linear term:

$$\tilde{a}_{(n)}(t) \approx B_{(ni)}p_{(i)}(t). \tag{10}$$

The elements of $B_{(ni)}$ are selected to minimize the mean square error, $e_{\tilde{a}_{(n)}} = \overline{\left[\tilde{a}_{(n)}(t) - a_{(n)}(t)\right]^2}$ by requiring that $\partial e_{\tilde{a}_{(n)}}/\partial B_{(ni)} = \partial\overline{\left[B_{(ni)}p_{(i)}(t) - a_{(n)}(t)\right]^2}/\partial B_{(ni)} = 0$. The solution to this minimization problem is a linear system of equations. The process begins off-line with an ensemble of "j" solutions. Each perturbation solution $\acute{u}^i_{(j)}(\boldsymbol{x},t)$ is projected onto "n" POD modes, $\acute{u}^i_{(j)}(\boldsymbol{x},t) = a_{(jn)}(t)\phi^i_{(n)}(\boldsymbol{x})$ where $a_{(jn)}$ is the coefficient corresponding to POD mode "n" from solution "j." With "i" surface pressure sensors, define a second-order tensor $p_{(ij)}$. Each entry consists of surface pressure at the "i" sensor location from the "j" solution. Define a second-order tensor $B_{(jn)}$ that satisfies the following:

$$p_{(ik)}p_{(jk)}B_{(jn)} = p_{(ik)}a_{(kn)}. \tag{11}$$

Define a vector $\tilde{p}_{(i)}(t)$ composed of instantaneous surface pressures at the "i" sensor locations and a vector $\tilde{a}_{(n)}(t)$ that satisfies the following:

$$\tilde{a}_{(n)}(t) = B_{(ni)}\tilde{p}_{(i)}(t). \tag{12}$$

Then, $\tilde{a}_{(n)}(t)$ are POD coefficients that approximate the instantaneous perturbation velocity:

$$\tilde{\acute{u}}^i(\boldsymbol{x},t) \approx \tilde{a}_{(n)}(t)\phi^i_{(n)}(\boldsymbol{x}). \tag{13}$$

State estimates from either the dynamical estimator or the measurement-based estimator (or both) will be used to approximate the performance output "in the loop." Substituting the low-dimensional velocity representation into (3) yields the output approximation:

$$F^1_{\mathrm{V}} = \varpi(c^{<1000\mathrm{V}>1} + d^{<1100\mathrm{V}>1}_{(\rho)}\zeta_{(\rho)} + c^{<1010\mathrm{V}>1}_{(\mu)}\dot{\eta}_{(\mu)} + C^{<1100\mathrm{V}>1}_{(m)}a_{(m)}). \tag{14}$$

$c^{<1000\mathrm{V}>1}$, $c^{<1010\mathrm{V}>1}_{(\mu)}$, $d^{<1100\mathrm{V}>1}_{(\rho)}$, and $C^{<1100\mathrm{V}>1}_{(m)}$ are integro-differential functions of velocity, computed off-line and only once, during the model construction step.

Before using them for control, estimators were constructed with data from the initial control simulation (with CFD-computed output in the loop), and their accuracies were evaluated. The left panel of Figure 5 compares time histories from the dynamical and measurement-based estimators over one pitching cycle (blue and green curves, respectively) with values obtained by projecting CFD solutions onto the POD eigenvectors (red curve). Comparisons are good with the exception of the measurement-based estimation of $a_{(2)}$, which captures the correct trend but is contaminated with measurement noise. The second POD mode contains only a small percentage of the perturbation energy—as evidenced by the much smaller maximum value in the right vertical axis—and the signal-to-noise ratio is commensurately small. The right panel of Figure 5 compares time histories of performance output (viscous force acting on the aperture surface) using the dynamical and measurement-based state estimates in the output approximation of (14) (blue and green curves, respectively) with CFD-computed values (red curve). Both low-dimensional approximations are reasonably accurate.

C. Regulators and Filters

With the control input defined as the time derivative of the unsteady jet ($\dot{u}$), a proportional-integral (PI) regulator is employed in the first set of control-in-the-loop simulations:

$$\dot{u}(t) = K_1\left[y(t) - y_T\right] + K_2\int_0^t \left[y(\tau) - y_T\right]d\tau, \tag{15}$$

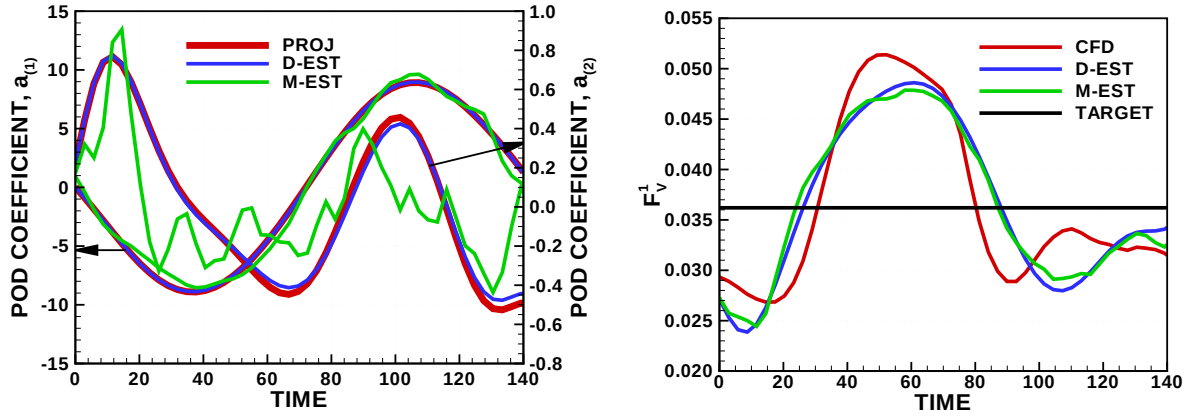

Figure 5. In the left panel, comparisons of dynamical and measurement-based state estimates (blue and green curves, respectively) with POD coefficients obtained by projecting CFD solutions onto the POD eigenvectors (red curve). Note that the left vertical axis is the first POD coefficient and the right the second with arrows indicating which curves correspond to the two axes. In the right panel, comparisons of performance output approximations using dynamical and measurement-based state estimates (blue and green curves) with CFD-computed output (red curves).

where K_1 and K_2 are the proportional and integral gains, respectively. The unsteady jet velocity is

$$u(t) = \int_0^t \dot{u}(\tau) d\tau, \tag{16}$$

providing the time-dependent boundary condition in the CFD model during the control simulations. Choosing $\dot{u}$—rather than u—as the control input has the advantage of "smoothing" the effective jet velocity (u) through the integration operation. The integral term provides additional smoothing of the input, and it also provides a phase shift between input and output. The initial control simulation with CFD-computed output in the loop yielded satisfactory results with the following gain constants: $K_1 = 5.0$ and $K_2 = 0.0$.

Adding a filter to a regulator produces a compensator, capable of "compensating" for both modeling uncertainties and measurement noise. Modeling uncertainties will exist in both the simulations and the experiments. Measurement noise in the CFD simulations, even with DES, is not large, but noise in the wind tunnel pressure measurements is, and a filter must be included in a controller that will operate effectively. A Kalman filter uses both the dynamical and measurement-based estimators jointly to offset errors from each. It weights contributions from the two sources of error in determining levels of compensation that are applied. In systems with low levels of measurement noise and higher levels of dynamical model uncertainty, filter parameters impose greater reliance on the measurement-based estimator and less on the dynamical estimator. In systems with more measurement noise, parameters impose less reliance on the measurements and more on the dynamical estimator.

Adding a continuous Kalman filter to the dynamical estimator in (8) yields

$$\dot{\hat{\boldsymbol{x}}} = \boldsymbol{a}_0 + \boldsymbol{A}_1\hat{\boldsymbol{x}} + \ \boldsymbol{b}_0 u + \boldsymbol{b}_2\dot{u} + \boldsymbol{b}_3\dot{\eta} + \boldsymbol{b}_4\ddot{\eta} + \ \boldsymbol{K}_f\left(\hat{\boldsymbol{x}}_m - \boldsymbol{H}\hat{\boldsymbol{x}}\right) \tag{17}$$

where $\boldsymbol{H}$ is a sensitivity term, defined here as the unity matrix and $\hat{\boldsymbol{x}}_m$ is the measurement-based state estimate. The Kalman gain, $\boldsymbol{K}_f(t)$, provides a means of weighting confidence in the measurement-based state estimate against confidence in the dynamical estimate. Large values of $\boldsymbol{K}_f(t)$ place more weight on the measurement-based estimate. As $\boldsymbol{K}_f(t)$ approaches zero, weighting of the dynamical estimate increases. The Kalman gain is defined as

$$\boldsymbol{K}_f = \boldsymbol{P}\boldsymbol{H}^T\boldsymbol{V}_s^{-1}. \tag{18}$$

$\boldsymbol{V}_s$ is the power spectral density of the error in measurement-based state estimates due to measurement noise:

$$\boldsymbol{V}_s = \boldsymbol{B}\boldsymbol{D}_z\boldsymbol{V}\boldsymbol{D}_z\boldsymbol{B}^T \tag{19}$$

where $\boldsymbol{V} = V_p\boldsymbol{I}$ is the power spectral density of the measurement noise. $\boldsymbol{D}_z$ is a diagonal matrix with diagonal entries equal to $\partial f/\partial z|_{z=p_0}$. $\boldsymbol{P}$ represents the covariance of the measurement-based and dynamical estimates and is determined from the Riccati equation:

$$\dot{\boldsymbol{P}} = \boldsymbol{A}_1\boldsymbol{P} + \boldsymbol{P}\boldsymbol{A}_1^T + \boldsymbol{W} - \boldsymbol{P}\boldsymbol{H}^T\boldsymbol{V}_s^{-1}\boldsymbol{H}\boldsymbol{P}. \tag{20}$$

$\boldsymbol{W} = W_p\boldsymbol{I}$ is the process noise power spectral density, representing modeling uncertainties.

Figure 6 describes the controller design and testing process: parallel paths that begin with the construction of estimators, filters, and regulators in Clear Science Corp.'s (CSC's) SMARTFLOW—using either computational or experimental data. These components are imported from SMARTFLOW to the Control toolbox of MATLAB® to compute gains and then imported from MATLAB® into either LabVIEW for control-in-the-loop wind tunnel runs or into the boundary condition subroutines of a CFD model for control-in-the-loop simulations. Computational demonstrations are described in the next section and experimental demonstrations in "Feedback Flow Control for a Three-Dimensional Turret (Part II)."

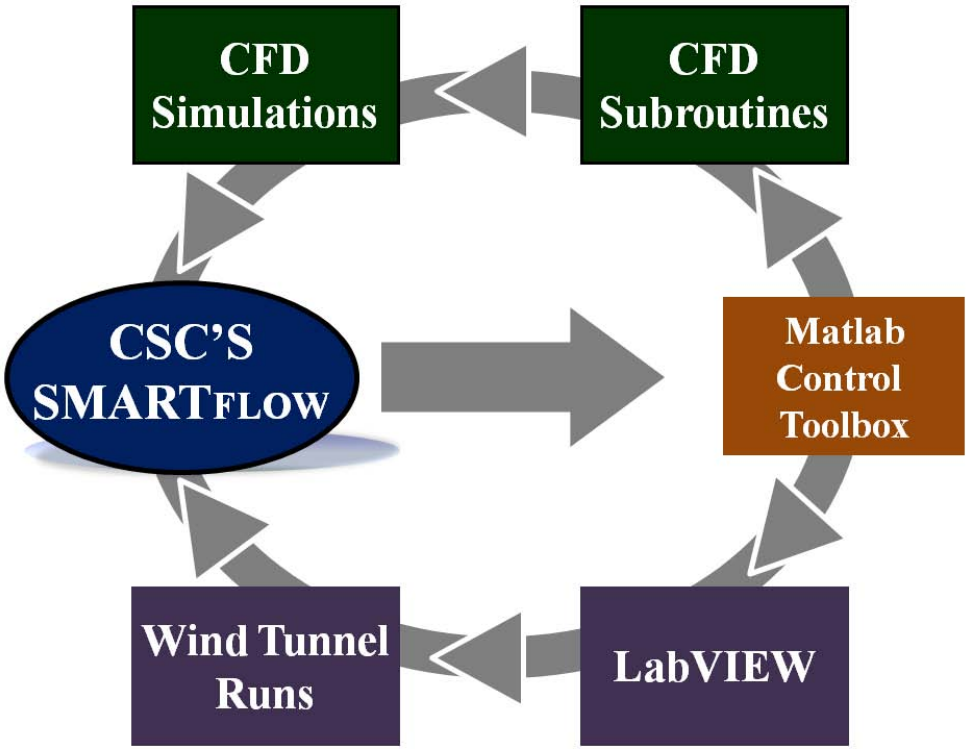

Figure 6. A flow chart of the controller design and testing process—parallel tracks beginning with Clear Science Corp.'s SMARTFLOW.

V. Feedback Control Simulations

Two sets of feedback control simulations were performed: without measurement noise and with measurement noise. In the latter, white noise is superposed on the surface pressure measurements at levels commensurate to noise in the wind tunnel tests in order to develop filter designs that will work effectively in the tunnel. Noise must be manually added to the surface pressure signals because DES is capable of capturing only the larger fluctuations in the flow—omitting the small-scale fluctuations that result in measurement noise. Because of this, root-mean-square (rms) values of velocity fluctuations are on the order of five times higher in the wind tunnel than in the detached-eddy simulations.

To define and quantify measurement noise, surface pressure is first decomposed into two parts, the true pressure signal $p_s(t)$ and a noise component $p_n(t)$: $p(t) = p_s(t) + p_n(t)$. The signal-to-noise ratio (SNR) is then defined as SNR $\equiv \langle p_s^2\rangle/\langle p_n^2\rangle$ where $\langle\cdot\rangle$ denotes time averaging. Noise levels in the simulation are matched to levels in the wind tunnel by examining the average surface pressure spectrum from a wind tunnel run.

The spectrum in Figure 7 is computed by averaging data from 18 pressure sensors in the wind tunnel model. Using a cut-off frequency of 500 Hertz, measurements above the cut off are considered noise, and the SNR is computed as the ratio of the area under the signal region to the area under the noise region (marked as green and grey, respectively, in Figure 7). Using the areas in Figure 7 yields a SNR of 3.77.

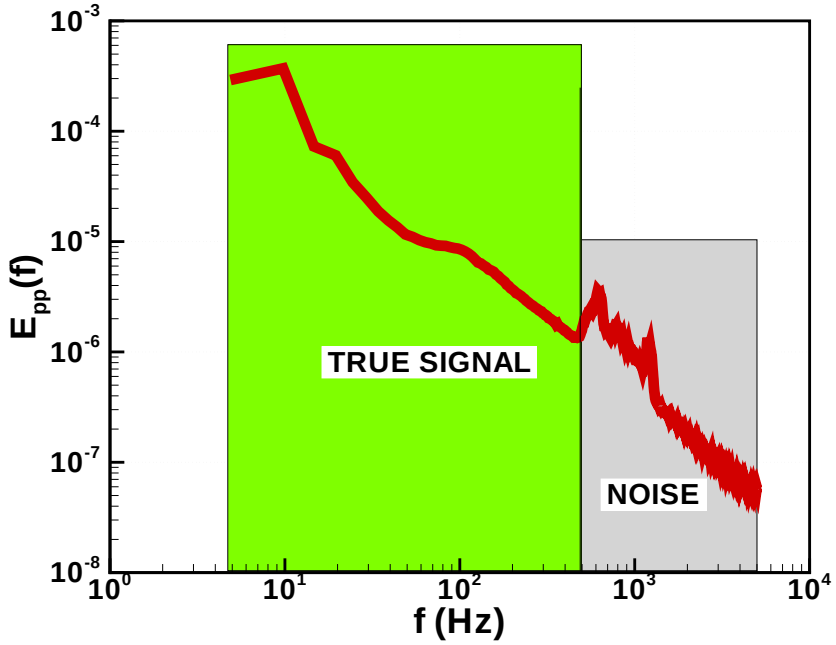

Figure 7. Quantification of the signal-to-noise ratio of surface pressures in the wind tunnel experiment. The pressure spectrum is computed with data from 18 sensors. A cut-off frequency of 500 Hertz separates the true pressure signal from the noise (marked as the green and grey regions, respectively.

Pressure measurements in the CFD simulations are modified to improve the condition number of the measurement estimator. The noise is defined as

$$p_n = \frac{|\hat{p}_1 - \hat{p}_2|}{R_N}\,\xi \tag{21}$$

where ξ is a random variate with zero mean and unit variance and $\hat{p}_{1,2}$ are pressure optima. Equating the different definitions of noise used in the simulations and the experiments, an experimental signal-to-noise ratio of 3.77 yields a CFD noise factor of $R_N \approx 4$. To ensure that noise levels are at least as high as noise in the wind tunnel, a value of $R_N = 5$ is prescribed for the control-in-the-loop CFD simulations.

In the first closed-loop-control simulation, noise is not added to the pressure measurements, and the Kalman filter is excluded from the controller. Figure 8 contains time histories of performance output (left) and control input (right) from the CFD simulation with no measurement noise. The PI regulator uses output approximations based on the measurement-based estimator exclusively, although CFD-computed values of output are included in order to evaluate controller performance. The estimator uses eight pressure sensors located on the turret surface. The green curve in the left panel of Figure 8 is from the open-loop simulation with a constant suction jet. The purple and black curves are from the model-in-the-loop simulation: purple, the CFD (plant) values of output and black, the model values from the measurement-based estimator (these are the values that the regulator uses to control). The grey curve is from the initial control simulation (also shown previously in Figure 4).

Comparing the black and purple curves, the model approximation of output does track the target value closely, but differences exist between the output approximation and plant values. Comparing the purple and green curves, the closed-loop controller provides modest improvements over open-loop control. Comparing the grey and purple curves, using plant values of output in the loop provides tighter control, which is

not unexpected. The right panel of Figure 8 compares control input (suction jet velocity) from the initial simulation with CFD-computed output in the loop (grey curve) with input from the model-in-the-loop simulation. Tighter control is achieved in the initial simulation through larger variations in suction velocity.

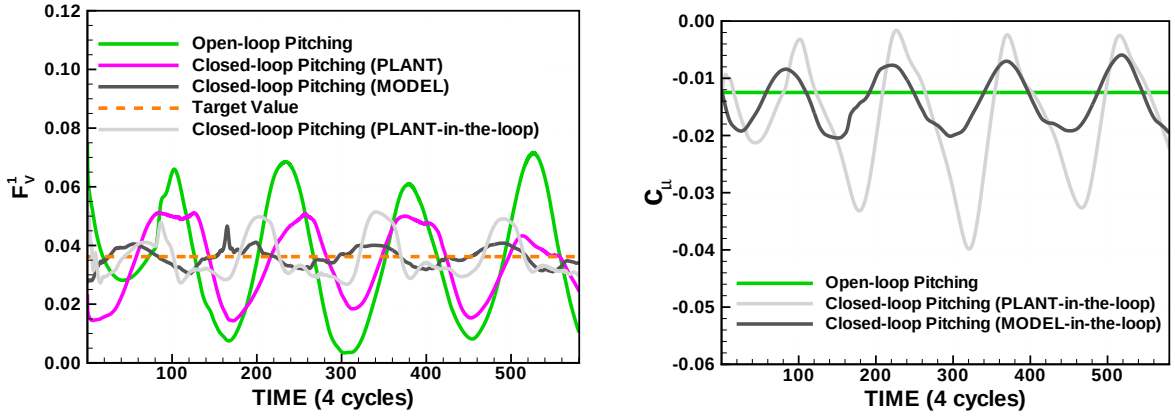

Figure 8. Time histories of performance output (left) and control input (right) from the CFD simulations with no measurement noise.

The next set of simulations includes measurement noise, and a Kalman filter is included in the controller. Three simulations were performed with measurement noise, and the parameters that were used in the simulations are listed in Table 1. The integral gain is set to zero and the proportional gain is 5 in each. Also, the noise factor (R_N) in each is 5.0, again, comparable to the noise levels in the pressure signals of the wind tunnel tests. The three simulations are distinguished by the assigned values of the filter parameters. The measurement covariance (V_p) appears in (20), the Riccati equation, through the power spectral density of error in (19), and the process covariance (W_p) and the measurement covariance appears in (20) through $\boldsymbol{W} = W_p \boldsymbol{I}$. The assigned measurement covariance is 0.003 in each simulation, but the process covariance is assigned as 10 in Run 1, 0.1 in Run 2 and 0.01 in Run 3. Higher values of W_p result in less reliance on (or confidence in) the dynamical estimator and more on the measurements. Therefore, Run 2 places less confidence in the (noisy) measurements than Run 1—and Run 3 even less.

Quantity	Symbol	Run 1	Run 2	Run 3
Proportional gain	K_1	5	5	5
Integral gain	K_2	0	0	0
Signal-to-Noise Ratio	R_N	5.0	5.0	5.0
Process covariance	W_p	10	0.1	0.01
Measurement covariance	V_p	0.003	0.003	0.003

Table 1. Parameter settings for the control runs with noise.

Figure 9 contains results from the simulations with measurement noise, along with results from the previous no-noise simulation for comparison. Time histories of output (viscous force on the aperture) from the plant (CFD model) are included in the left panel. These reflect the actual performance of the controllers. Time histories of the output from the estimators are included in the right panel. These are the values that the controllers use to track the output. Comparing the red, green, and orange curves of the right panel indicates that Run 2 does a much better job of filtering the measurement noise than Run 1, and Run 3 does better yet—obviously because the filter is tuned to do so. Comparing the red, green, and orange curves in the left panel, this results in much better controller performance—with Run 3 performing best.

The left panel of Figure 10 contains time histories of control input (jet momentum coefficients) from the same set of runs. From the red curve, Run 1 expends more energy in suction even though its performance is poor, highlighting the fact that the Kalman filter can work but must be properly calibrated. The right panel of Figure 10 contains time histories of fluctuating velocity (u_{rms}) integrated over a volume of the aperture

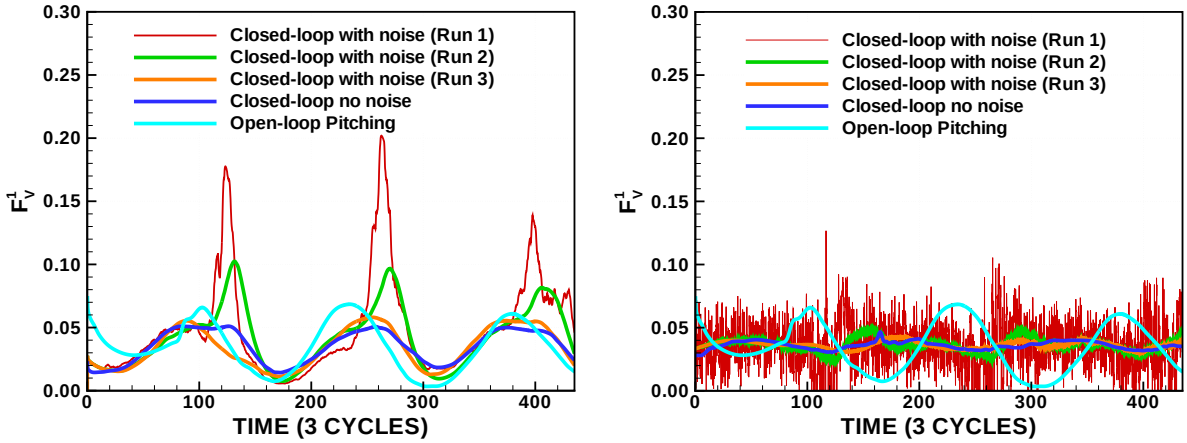

Figure 9. Time histories of output from the control-in-the-loop CFD simulations with measurement noise. Results from the simulation with no noise are included for comparison. Output from the plant (CFD model) in the left panel and output from the estimator in the right panel.

field of view adjacent to the aperture surface. The extent of control effectiveness of the suction jets is limited to a region near the surface. From the figure, baseline fluctuations in the flow over a stationary turret with no control are 0.1 m/s (black curve), and average fluctuations over a pitching turret with no control are about the same (brown curve). Both the closed- and open-loop controllers reduce average values to approximately 0.06 (blue and cyan curves, respectively). No measurement noise has been added in these two control simulations. The blue and cyan curves in the left panel of Figure 9 show that tracking of integrated shear stress is slightly tighter with closed-loop control than with open loop, but the blue and cyan curves in the right panel of Figure 10 reveal that control of $u_{\rm rms}$ is about the same. Tracking $u_{\rm rms}$ directly, rather than integrated shear stress, would be a logical next step, and this step is taken in the advanced controller design for the wind tunnel as described in "Feedback Flow Control for a Pitching Turret (Part II)."

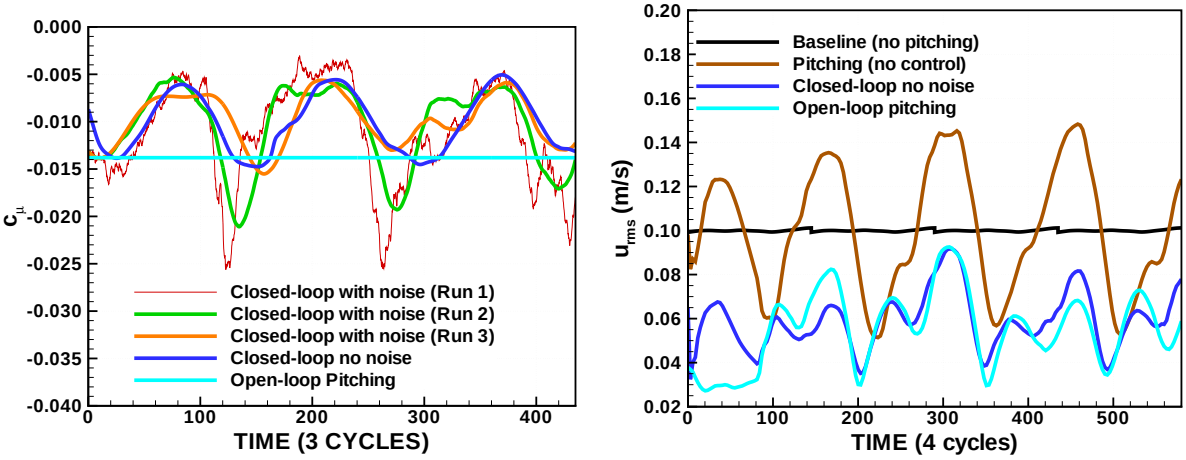

Figure 10. Time histories of input from the control-in-the-loop CFD simulations with measurement noise (left panel). Results from the simulation with no noise are included for comparison. Time histories of $u_{\rm rms}$ integrated over a volume of the aperture field of view adjacent to the aperture (right panel).

To compare the cost-effectiveness of closed-loop control, the quantity $\langle c_\mu \rangle$ provides a measure of the energy requirements for control (the jet momentum coefficient integrated over time), and the quantity (α) is a measure of the energy savings of closed-loop control over open-loop:

$$\langle c_\mu \rangle = \frac{1}{T}\int_0^T c_\mu(t)dt \quad \text{and} \quad \alpha = \frac{|\langle c_\mu \rangle|_{\rm open-loop} - |\langle c_\mu \rangle|}{|\langle c_\mu \rangle|_{\rm open-loop}} \times 100\%. \tag{22}$$

Table 2 summarizes the results. The simulation with measurement noise and a heavy reliance on the dynamical estimator (Run 3) provides the greatest savings: 28.2%.

Run	Energy Cost ($\langle c_\mu \rangle$)	Cost Savings (α) %
Closed-loop with Noise (Run 1)	-0.0114	17.4
Closed-loop with Noise (Run 2)	-0.0106	23.1
Closed-loop with Noise (Run 3)	-0.0099	28.2
Closed-loop with no Noise	-0.0102	26.1
Open-loop	-0.0138	–

Table 2. Energy costs and the cost savings of closed-loop control over open-loop.

VI. Conclusion

Closed-loop systems for controlling flow separation and turbulence above a pitching turret have been developed and tested through a series of control-in-the-loop CFD simulations and wind tunnel runs. Controller designs and the computational tests have been described here, and wind tunnel tests are described in the companion paper, "Feedback Flow Control for a Pitching Turret (Part II)." Levels of flow separation and turbulence change as the turret pitches, and the systems successfully reduce these levels in the dynamic environment through feedback control—meeting the objective of control in the presence of disturbances over a range of operating conditions. Another objective is the minimization of control input: achieving threshold levels of control with less actuator energy. Closed-loop systems in the CFD simulations reduce actuation requirements by as much as 28% over open-loop controllers while meeting or exceeding the open-loop performance. Closed-loop controllers offer comparable cost savings over open-loop control in the wind tunnel tests that are described in the companion paper, "Feedback Control for a Pitching Turret (Part II)."

Acknowledgments

This material is based upon work supported by the US Air Force Research Laboratory's Air Vehicles Directorate under Contract FA8650-08-C-3827. Any opinions, findings, conclusions, or recommendations expressed in the material are those of the authors and do not necessarily reflect the views of the US Air Force.

References

[1]A. M. Nightingale, B. Goodwine, M. Lemmon, and E. J. Jumper, "Feed-forward Adaptive-Optic System Identification Analysis for Mitigating Aero-Optic Disturbances," AIAA Paper 2007-4013, *38th AIAA Plasmadynamics and Lasers Conference*, Miami, FL, 2007.

[2]S. Gordeyev, T. E. Hayden, and E. J. Jumper, "Aero-Optical and Flow Measurements Over a Flat-Windowed Turret," *AIAA Journal*, Vol. 45, No. 2, 2007, pp. 347-357.

[3]B. Vukasinovic, and A. Glezer, "Control of a Separating Flow over a Turret," *37th AIAA Fluid Dynamics Conference*, AIAA Paper 2007-4506, Miami, Florida, 2007.

[4]M. Y. Andino, R. D. Wallace, R. F. Schmit, R. C. Camphouse, J. H. Myatt, and M. N. Glauser, "Flow and Aero-Optics Around a Turret Part I: Open Loop Flow Control," AIAA Paper 2008-4216, *4th Flow Control Conference*, Seattle, WA, 2008.

[5]M. Glauser, H. Higuchi, J. Ausseur, J. Pinier, and H. Carlson, "Feedback Control of Separated Flows," AIAA Paper 2004-2521, *2nd AIAA Flow Control Conference*, Portland, OR, 2004.

[6]J. T. Pinier, J. M. Ausseur, M. N. Glauser, and H. Higuchi, "Proportional Closed-Loop Feedback Control of Flow Separation," *AIAA Journal*, **45**, No. 1, 2007, pp. 181-190.

[7]R. D. Wallace, M .Y. Andino, M. Glauser, R. C. Camphouse, R. F. Schmit, and J. H. Myatt, "Flow and Aero-Optics Around a Turret Part II: Surface Pressure Based Proportional Closed Loop Flow Control," AIAA Paper 2008-4217, *4th Flow Control Conference*, Seattle, WA, 2008.

[8]A. J. Smits and J -P. Dussauge, Turbulent Shear Layers in Supersonic Flow, 2nd Edition, Springer 2006.

[9]P. R. Spalart, W. H. Jou, M. Strelets and S. .R. Allmaras, "Comments on the feasibility of LES for wings and on a hybrid RANS/LES approach," 1st AFOSR Int. Conf. on DNS/LES, Aug. 4-8, 1997, Ruston, LA. In: Advances in DNS/LES, C. Liu and Z. Liu Eds., Greyden Press, Columbus, OH, USA (1997).

[10]K. D. Squires, "Detached-Eddy Simulation: Current Status and Perspectives," In: R. Friedrich, B. J. Gurts, O. Metaism, (Eds.),*Direct and Large Eddy Simulation*, **5**, Kluwer, Dordrecht, 2004, pp. 465–480.

[11]R. T. Biedron and C. L. Rumsey, CFL3D Version 5.0 User's Manual, NASA Langley Research Center, Aerodynamic and Acoustic Methods Branch, Hampton, VA.

[12]P. R. Spalart and S. R. Allmaras, " A one equation turbulence model for aerodynamic flows", *La Recherche Aerospatiale*, **1**, pp. 5–21 (1994).

[13]J. L. Lumley, "The structure of inhomogeneous turbulent flows," Atmospheric Turbulence and Radio Wave Propagation, ed. A. M. Yaglom and V. I. Tatarski, Moscow: Nauka, 1967, pp. 166–178.

[14]R. J. Adrian, "On the role of conditional averages in turbulence theory," In *Turbulence in Liquids; Proceedings of the Fourth Biennial Symposium on Turbulence in Liquids*, J. Zakin and G. Patterson (Eds.), Science Press, Princeton, 1977, pp. 323–332.

[15]H. Carlson and R. Miller, "Reduced-order Modeling and Sensing of Flow Separation on Lifting Surfaces," AIAA Paper 2002-0975, 40th AIAA Aerospace Sciences Meeting & Exhibit, Reno, NV, January, 2002.